Journal of Civil, Construction and Environmental Engineering
2026, Vol. 11, No. 4, pp. 214–224
https://doi.org/10.11648/j.jccee.20261104.16

Research Article

UAV-Based Photogrammetric Inspection of an Urban Bridge in a Lagoonal Environment: Case Study of the Old Cotonou Bridge

Kora Farid Carlos Yarou*, Valery Kouandete Doko, Boris Ganmavo, Thede Agbelele, Mohamed Gibigaye

Civil Engineering Department, University of Abomey-Calavi, Abomey-Calavi, Benin

Abstract

Bridge infrastructure in sub-Saharan Africa is often monitored with limited resources, leaving many ageing structures without a reliable geometric baseline for tracking deterioration. This paper reports on a UAV photogrammetric inspection campaign conducted on the Old Cotonou Bridge, a two-lane reinforced concrete structure crossing the coastal lagoon of Cotonou (Benin), with the aim of establishing a quantitative geometric reference for deck deformation monitoring. A flight of 573 images was captured at 56.1 m altitude using a DJI Mavic 2 Pro equipped with a Hasselblad L1D-20c 20 Mpx sensor (GSD: 1.28 cm/px), and the dataset was processed with Agisoft Metashape Professional 2.3.1 following a Structure-from-Motion and Multi-View Stereo workflow. Processing yielded a dense point cloud of 26.8 million points at 383 pts/m^2, a DEM at 5.11 cm/px, and a georeferenced orthomosaic in WGS 84 / UTM zone 31N; six thematic classes were identified by automatic classification, followed by manual verification of the Road and Building classes. Deck deformation was then quantified through 2D polynomial regression of the deck surface, revealing seven statistically significant depression zones (D1–D7) with amplitudes ranging from −17.3 cm to −79.4 cm relative to the reference surface, over areas of 2 to 30 m^2. The vertical accuracy achieved (RMSE Z = 0.44 cm) confirms that UAV photogrammetry can reliably serve as a quantitative tool for structural deformation detection on bridge decks, despite the use of only three Ground Control Points. The geometric reference dataset (T) produced here places at the disposal of asset managers a georeferenced database that is immediately usable for prioritising maintenance interventions on this and comparable structures.

Keywords

Unmanned Aerial Vehicle Photogrammetry, Dense Point Cloud, Deformation Detection, Bridge Inspection, Light Detection and Ranging Classification, Orthomosaic, Structure-from-Motion

1. Introduction

Bridge infrastructure plays a central role in the transport networks of sub-Saharan African countries, where service continuity directly conditions economic activity and population mobility. The Old Cotonou Bridge, a mid-20th century reinforced

*Correspondence: Kora Farid Carlos Yarou (faridyarou3009@gmail.com)

Received: 30 June 2026; **Accepted:** 13 July 2026; **Published:** 28 July 2026

concrete structure spanning the coastal lagoon of Cotonou (Benin), remains in active service despite increasing deterioration due to marine corrosion, traffic overloads, and the absence of systematic monitoring. Diagnosing such ageing infrastructure represents a major challenge for asset managers in developing countries with limited inspection resources.

Traditional visual inspection methods suffer from well-documented limitations: assessor subjectivity, restricted access to under-deck zones, and the absence of quantitative geometric data [1]. Over the past decade, UAVs combined with Structure-from-Motion (SfM) photogrammetry and dense image matching have emerged as a viable non-intrusive alternative [2]. Nex and Remondino [3] demonstrated that UAV-based surveys can achieve vertical accuracies of 1–2 times the GSD, while Ellenberg et al. [4] and Khaloo et al. [5] established their effectiveness for crack detection and surface damage assessment on bridge decks. In resource-constrained settings typical of many developing countries, low-cost SfM photogrammetry from consumer-grade drones has been shown to provide an accurate and affordable alternative to conventional surveying equipment [6]. For quantitative deformation analysis, Wheaton et al. [7] introduced the DEM of Difference (DoD) framework, later extended by Lague et al. [8] through the M3C2 method, which computes centimetric-precision signed distances between point clouds without requiring a prior reference state. Remondino et al. [9] further confirmed that Dense Image Matching can rival LiDAR accuracy at sufficient point densities. More recently, dedicated UAS-assisted inspection protocols [11] and non-destructive UAV-based structural health monitoring workflows [12] have extended these methods to a wider range of structures, while deep-learning-assisted UAV surveys have improved automated crack detection on concrete bridge decks [13]. Under controlled loading, UAV photogrammetry has achieved sub-millimetric displacement detection on instrumented reinforced concrete bridges [14], and full-scale photogrammetric deformation tracking has been demonstrated on an in-service highway bridge under controlled static load testing, achieving millimetric accuracy [15]. Field-oriented drone inspection protocols have likewise been reported directly on concrete and timber highway bridges, using object-based image analysis to segment deterioration on the deck surface [17], routine on-site UAV inspection workflows [18], and evaluated 3D reconstructions for damage localisation [19].

This study demonstrates the capacity of UAV photogrammetry to deliver quantitative structural diagnostics for the Old Cotonou Bridge. The objectives are: (i) to generate a georeferenced dense point cloud, orthomosaic and DEM from a single flight; (ii) to classify the point cloud using the ASPRS standard; and (iii) to detect deck deformation zones via 2D polynomial regression. Results show a vertical accuracy of 0.44 cm (RMSE Z) and seven statistically significant depression zones (D1–D7), with amplitudes from −17.3 cm to −79.4 cm over areas of 2 to 30 m^2, four of which exceed the 2σ threshold and require priority structural intervention, establishing the first geometric reference state (T_0) of the bridge for maintenance planning.

2. Materials and Methods

2.1. Structure Presentation

The Old Cotonou Bridge is a reinforced concrete under-roadway twin-girder structure, 380 m long, comprising 30 simply supported spans of 12.6 m, resting on two abutments and 29 intermediate piers. The deck is 11 m wide overall, with a carriageway of 2 × 3.70 m, flush strips of 0.25 m on each side, footways of 1.50 m, and S8-type guardrails. The study area covers 0.118 km^2 in WGS 84 / UTM zone 31N (EPSG: 32631), centred on E 438 300, N 702 920.

Figure 1. *View of the Old Cotonou Bridge crossing the Cotonou Lagoon.*

2.2. Materials

2.2.1. UAV Platform and Sensor

The survey was carried out using a DJI Mavic 2 Pro quadrotor drone equipped with its integrated Hasselblad L1D-20c camera (equivalent focal length 10.26 mm), of resolution 5,472 × 3,648 px and physical pixel size 2.41 µm. In-situ calibration was performed by bundle adjustment (Table 1).

Table 1. *Intrinsic calibration parameters of the Hasselblad L1D-20c sensor (DJI Mavic 2 Pro) obtained by bundle adjustment.*

Parameter	Value	Parameter	Value
F (px)	4,423.04	K1	0.00709
Cx (px)	−5.75	K2	0.00134
Cy (px)	−136.40	K3	−0.00407
P1	−0.000263	P2	−0.00141

F: focal length in pixels; Cx, Cy: principal point offsets; K1–K3: radial distortion; P1–P2: tangential distortion.

2.2.2. Flight Plan and Acquisition Protocol

The chosen flight plan is a parallel-strip (lawnmower) pattern, with a cruising altitude of 56.1 m above the lagoon water surface. Front and side overlap were set at a minimum of 80% and 70% respectively, with the camera pointing permanently at nadir. A total of 573 images were acquired in a single flight (Figure 2).

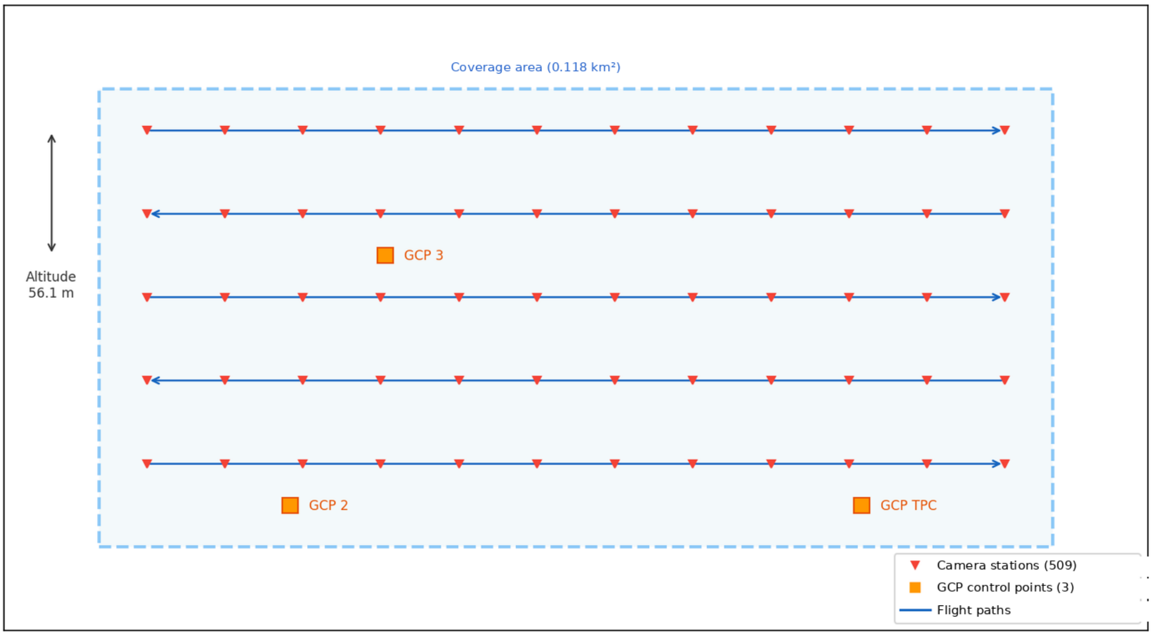

Figure 2. Parallel-strip flight plan and positions of the 509 aligned camera stations with the 3 Ground Control Points (GCPs).

2.2.3. Ground Control Points (GCPs)

Three coded targets, materialised by 0.5 m × 0.5 m painted slabs, were measured by GNSS in RTK mode (WGS 84 / UTM 31N): one in the central deck zone (GCP 2), one on the East bank (GCP 3) and one on the West bank (GCP TPC). This total of three falls below the recommended minimum of six points [4], which limits absolute planimetric accuracy, although the vertical component remains satisfactory as discussed in Section 3.1.3.

2.3. Methodology

2.3.1. Photogrammetric Processing Pipeline

All processing was performed with Agisoft Metashape Professional 2.3.1 [10] on a workstation equipped with an Intel Core i7-9700KF at 3.60 GHz, 16 GB RAM, and an NVIDIA GTX 1060 GPU. The complete processing chain is shown in Figure 3. The alignment step retained 509 of the 573 images (88.8%) and generated 266,227 tie points with an RMS reprojection error of 1.40 px. The dense reconstruction, derived from 504 depth maps at "Medium" quality with "Mild" filtering, yielded a cloud of 26.8 million points.

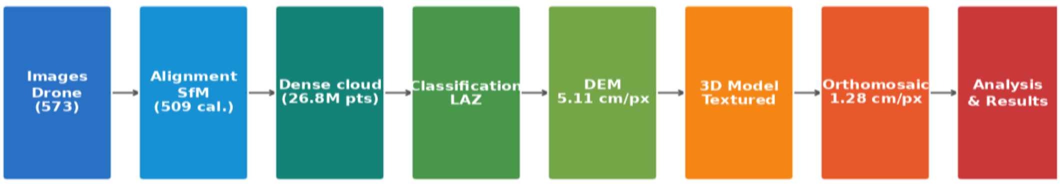

Figure 3. Complete photogrammetric processing pipeline, from raw images to final products.

2.3.2. Analysis and Deformation Detection Method

Deck deformation quantification followed a four-step protocol. First, points belonging to classes 11 (Road) and 6 (Building) were isolated and filtered by altitude (Z range: 4.7–6.2 m), then reprojected into a local frame (longitudinal axis s, transverse axis t) defined by Principal Component Analysis

(PCA) applied to the X, Y coordinates of the cloud. Second, a regular grid with 2 m × 0.5 m cells was built over the deck footprint; each cell takes as its value the median of the Z altitudes of the points it contains. The trend surface — representing the expected geometry of an undeformed deck — was then modelled by a bivariate second-degree polynomial ($z = a_0 + a_1s + a_2t + a_3s^2 + a_4st + a_5t^2$) fitted by least squares. A second-degree bivariate polynomial was chosen because simply-supported, constant-cross-section spans such as those of the Old Cotonou Bridge typically exhibit an approximately parabolic-to-linear longitudinal deck profile under self-weight and thermal effects, while genuine local damage (settlements, potholes) appears as short-wavelength residuals superimposed on this smooth trend rather than as part of it. Finally, residuals between the observed grid and this surface were computed: cells whose deviation exceeds 1.5σ or 2σ of the global standard deviation were retained as anomalous deformation zones.

3. Results and Discussion

3.1. Photogrammetric Products

3.1.1. Orthomosaic

The orthomosaic produced (Figure 4) covers the entire survey area (0.118 km^2) with a resolution of 1.28 cm/px in WGS 84 / UTM 31N. As a practical reference, a group of 2–3 pixels corresponds to 2.5–4 cm on the ground, making cracks wider than 3 mm and surface spalling visible to the naked eye. On the image, the two parallel decks, the intermediate piers standing in the lagoon, the traffic ramps on each bank, and several dark patches indicating advanced carriageway deterioration are all unambiguously identifiable.

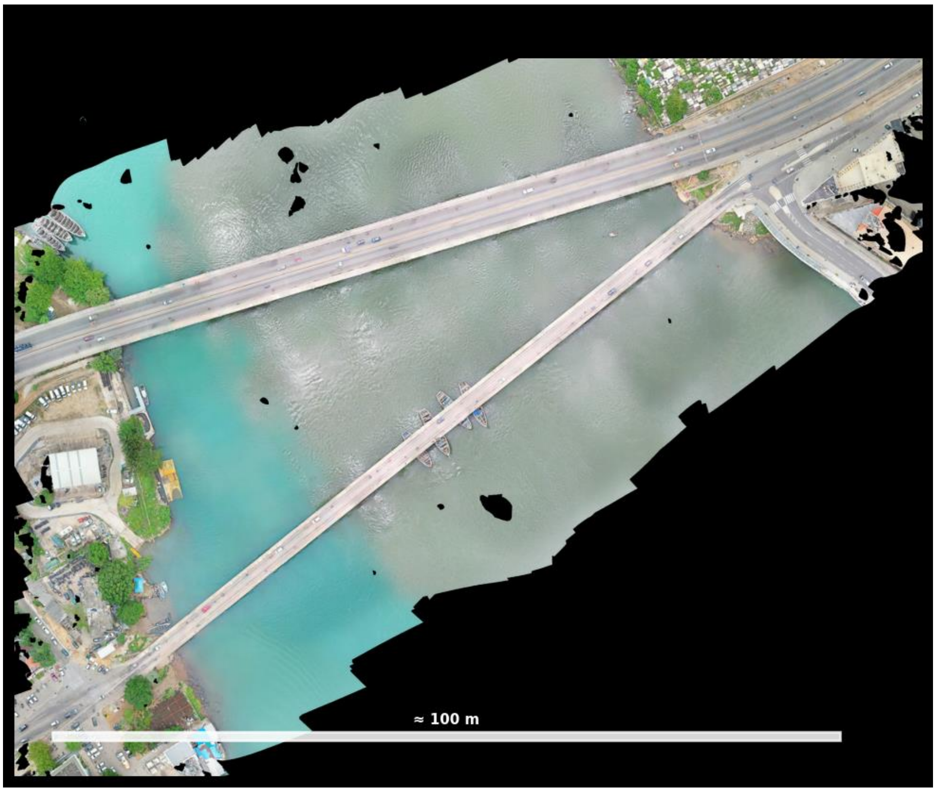

Figure 4. Georeferenced orthomosaic of the Old Cotonou Bridge (resolution: 1.28 cm/px; extent: 0.118 km^2). Source: Agisoft Metashape 2.3.1 [10], DJI imagery, 17 June 2026.

3.1.2. Classified Point Cloud

The 26.8 million-point cloud was subjected to Metashape's automated classification procedure, which distributed returns into six thematic classes (Table 2, Figure 5). The Road (34.1%) and Building (27.6%) classes together account for 61.7% of the total count and gather the structural elements of the bridge. The density of 383 pts/m^2 substantially exceeds the 10 pts/m^2 minimum prescribed by AASHTO for this type of inspection, ensuring reliable geometric representation at centimetric scale. The automated Road and Building classes produced by Metashape were subsequently checked and locally corrected by manual verification against the orthomosaic, in order to remove residual misclassifications (e.g. vehicles or vegetation fragments) before the deformation analysis described in Section 2.3.2.

Table 2. Automatic classification of the dense point cloud (ASPRS standard, Agisoft Metashape 2.3.1 [10]).

ASPRS Class	Label	No. of points	Prop. (%)	Structural role
2	Ground	5,845,879	21.7	Lagoon bottom
3	Artifact	299,630	1.1	Markers, furniture
5	High veg.	4,161,250	15.5	Trees, banks
6	Building	7,422,704	27.6	Bridge structures
11	Road	9,154,924	34.1	Deck, carriageway
?	Vehicle	2,318,542	8.6	Vehicles in transit
TOTAL	—	26,884,387	100.0	—

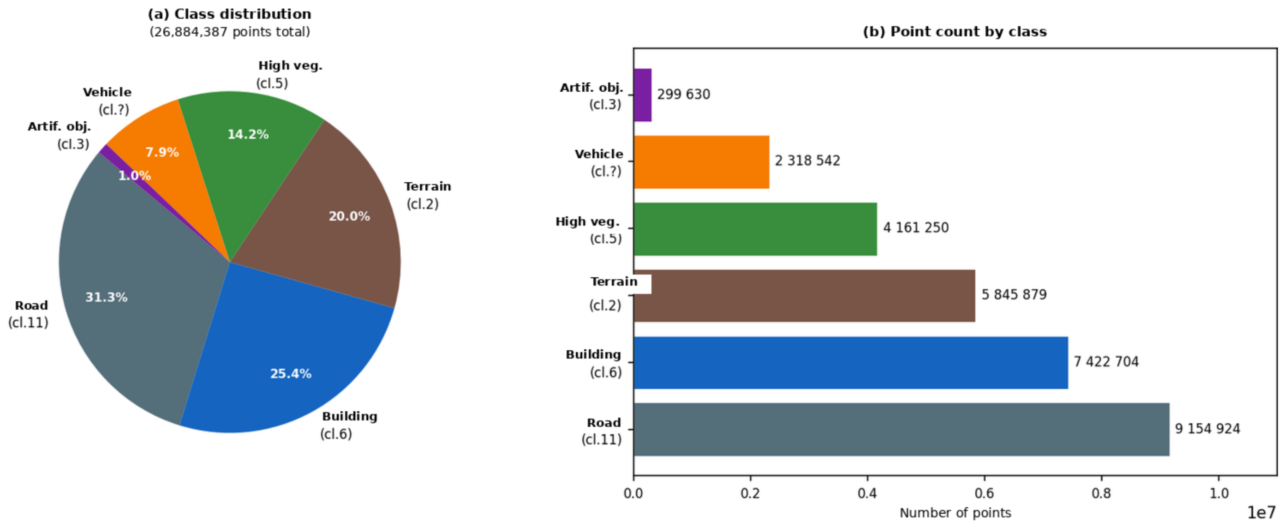

Figure 5. Distribution of the 26,884,387 points in the classified cloud (ANCIEN_PONT_C.laz). (a) Pie chart by class; (b) bar chart of point counts.

3.1.3. Geodetic Accuracy

GCP residuals are reported in Table 3 and Figure 6. The overall RMSE reaches 5.30 cm, but the vertical error is considerably better, at 0.44 cm (0.34 times the GSD). This discrepancy between the Z component and the planimetric component (RMSE XY = 5.28 cm) is a common feature of UAV photogrammetric surveys conducted without on-board PPK or RTK correction: altitude benefits from greater geometric redundancy than position in plan. For the vertical deformation analyses that follow, this Z accuracy is entirely sufficient as long as displacements exceed approximately 1.3 cm (three times RMSE Z).

Table 3. Ground Control Point residuals.

Point	Err. X (cm)	Err. Y (cm)	Err. Z (cm)	Err. XY (cm)	Total (cm)
GCP 2	−3.763	6.414	0.459	7.439	7.451
GCP 3	1.840	−2.558	−0.372	3.149	3.173
GCP TPC	1.939	−3.840	−0.492	4.299	4.330
RMSE	2.665	4.562	0.444	5.283	5.302

X = Easting, Y = Northing, Z = Elevation — WGS 84 / UTM 31N

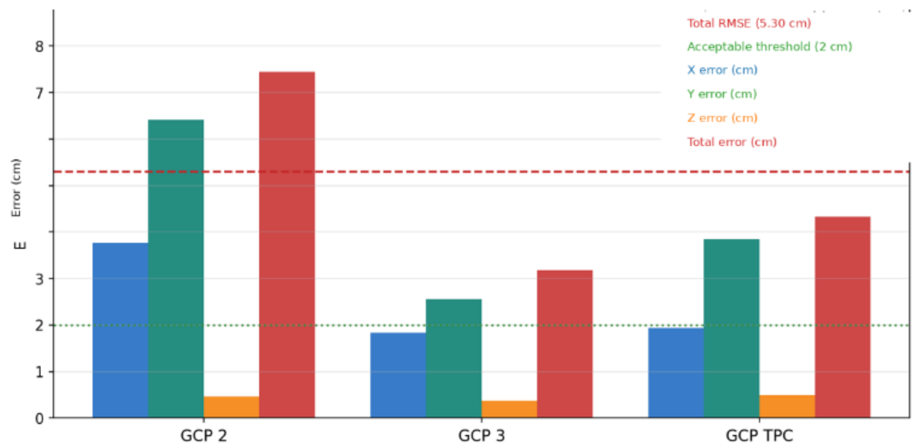

Figure 6. GCP residuals by component. The green dashed line marks the recommended quality threshold of 2 cm.

3.2. Detection and Characterisation of Deck Deformations

3.2.1. Longitudinal Elevation Profile

The longitudinal elevation profile of the deck, computed by sliding median on 3 m slices (119 bins, 686,293 Road-class points), is shown in Figure 7 with its fitted polynomial trend surface. Deviations range from −28.0 cm to +37.7 cm, with a standard deviation of 10.7 cm; such amplitude is far from what one would expect of a deck in good condition and reflects a pronounced geometric surface irregularity.

On the longitudinal profile (Figure 7b), 22 local troughs were identified, including two particularly marked depressions at s = −99 m (−28.0 cm) and s = −81 m (−27.7 cm). These troughs recur at an average spacing of approximately 18 m, slightly larger than the theoretical pier spacing (12.6 m), suggesting that each pier locally induces a differential settlement relative to the adjacent span. Such a periodic signal is typical of a progressive loss of bending stiffness in the structure.

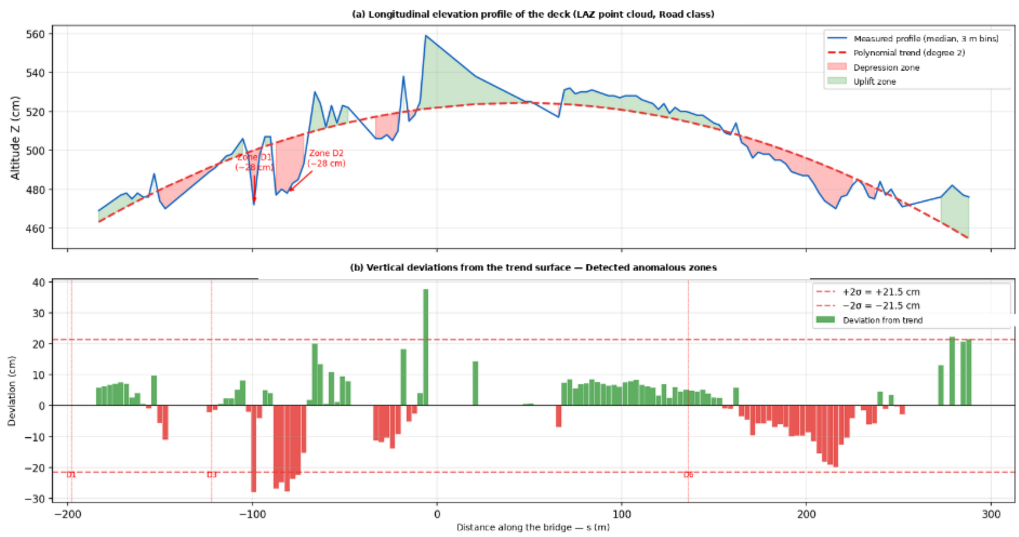

Figure 7. Longitudinal profile analysis of the bridge deck.(a) Measured elevation profile and polynomial trend surface; (b) Vertical deviations (green = uplift, red = depression). The ±2σ = ±21.5 cm limits are shown as red dashed lines.

3.2.2. Two-Dimensional Deformation Map

The plan-view map of residuals (Figure 8, grid of 2,459 valid cells) usefully complements the longitudinal analysis. The distribution of deviations broadly follows a normal law, with zero mean and a standard deviation of 10.74 cm. However, the distribution tails extend asymmetrically: while the positive maximum reaches +88.0 cm, the negative minimum descends to −79.4 cm. This negative-side asymmetry confirms that localised subsidence is statistically more pronounced than uplifts, indicating a preferential degradation mode in depression.

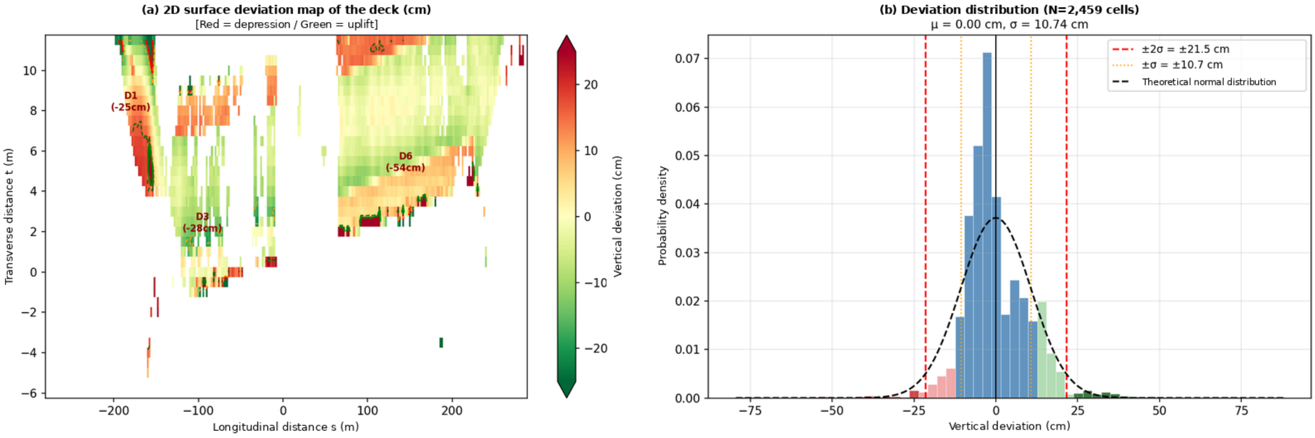

Figure 8. *2D surface deviation map of the bridge deck (cm) and statistical distribution of residuals. (a) Plan view (red = depression, green = uplift); (b) Residuals histogram with theoretical normal distribution superimposed.*

3.2.3. Geographic Location of Anomalous Zones

Figure 9 overlays the cells in significant depression (residuals < −1.5σ, i.e. 78 cells) on the georeferenced orthomosaic. Three sectors concentrate most of these anomalies: the western part of the bridge near s ≈ −185 m, the central zone near s ≈ −94 m, and the eastern section near s ≈ +145 m and +184 m. The comparison with the orthomosaic is particularly informative: several cells coincide with dark patches or crack networks visible to the naked eye on the image, corroborating the geometric interpretation with direct visual observation.

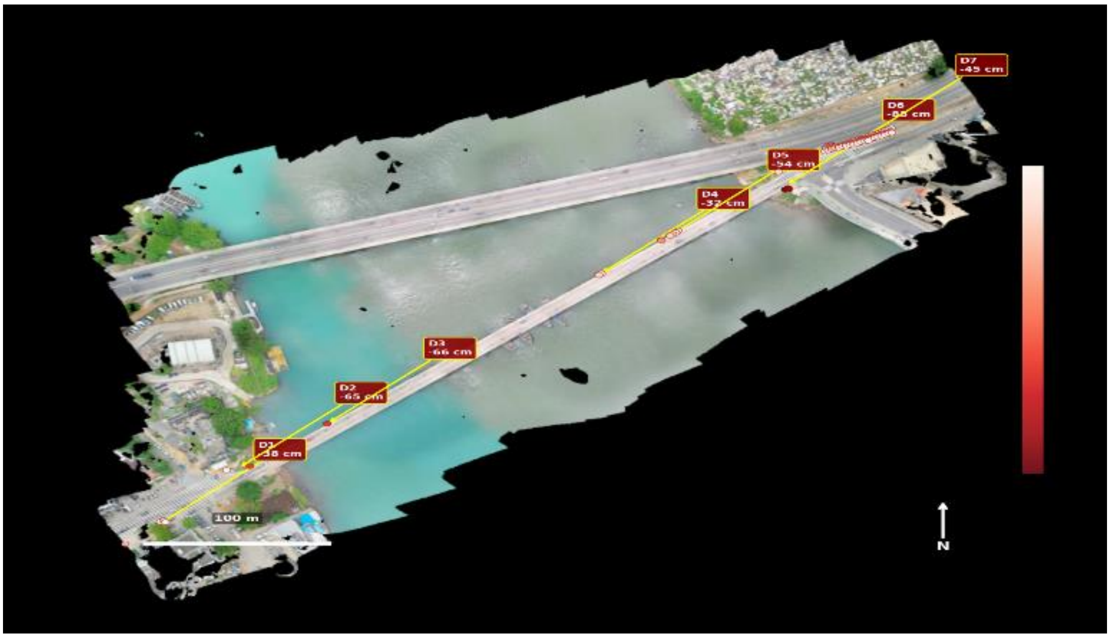

Figure 9. *Geographic location of deformation zones (red points: depression > 1.5σ) overlaid on the 1.28 cm/px orthomosaic. Zones D1, D3 and D6 are annotated with their maximum depression values.*

3.2.4. Transverse Profiles at Characteristic Cross-Sections

Figure 10 presents the transverse profiles at three sections: one undamaged (s = +50 m) and two deformed (s = −99 m for D3 and s = −180 m for D1). These cross-sections, perpendicular to the bridge axis, reveal measurable differential edge settlements at the deformed sections.

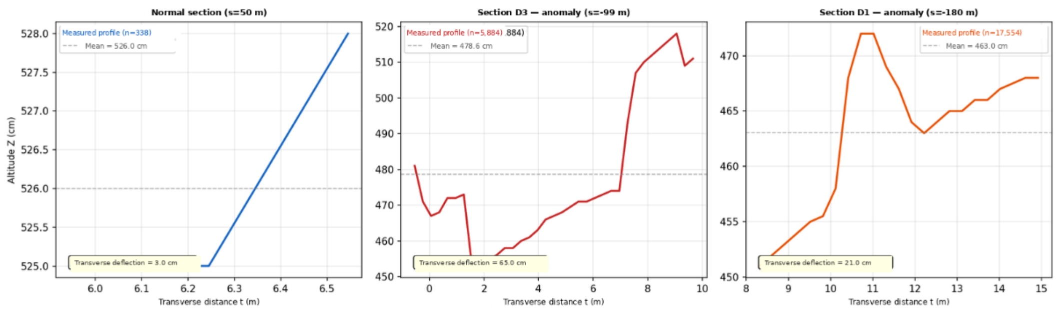

Figure 10. Transverse profiles at three characteristic cross-sections. Undamaged section (s = +50 m) and anomalous sections D3 (s = −99 m) and D1 (s = −180 m). The measured transverse deflection is indicated for each section.

3.2.5. Summary and Classification of Deformation Zones

In total, seven statistically significant depression zones (D1–D7) have been delineated and characterised (Table 4, Figure 11). Four of them — D2, D3, D6 and D7 — exceed the 2σ threshold (21.5 cm) and are retained as severe anomalies. D3 extends over 30 m^2 with a maximum amplitude of 54.4 cm, while D7 reaches 79.4 cm over only 3 m^2, making it the deepest point-localised depression in the structure.

Table 4. Inventory of depression zones detected on the deck of the Old Cotonou Bridge.

Zone	Position s (m)	Max. dep. (cm)	Area (m^2)	Threshold	Interpretation
D1	−198 to −180	−25.5	11	1.5σ	Span settlement
D2	−166 to −152	−34.1	19	2σ	Surface degradation
D3	−122 to −66	−54.4	30	2σ	Diff. settlement (pier)
D4	−34 to −30	−20.8	6	1.5σ	Local irregularity
D5	−12 to −10	−17.3	2	1.5σ	Local irregularity
D6	+136 to +154	−54.3	7	2σ	Diff. settlement (pier)
D7	+180 to +188	−79.4	3	> 2σ	Critical priority zone

reference state: T_0 = 17 June 2026

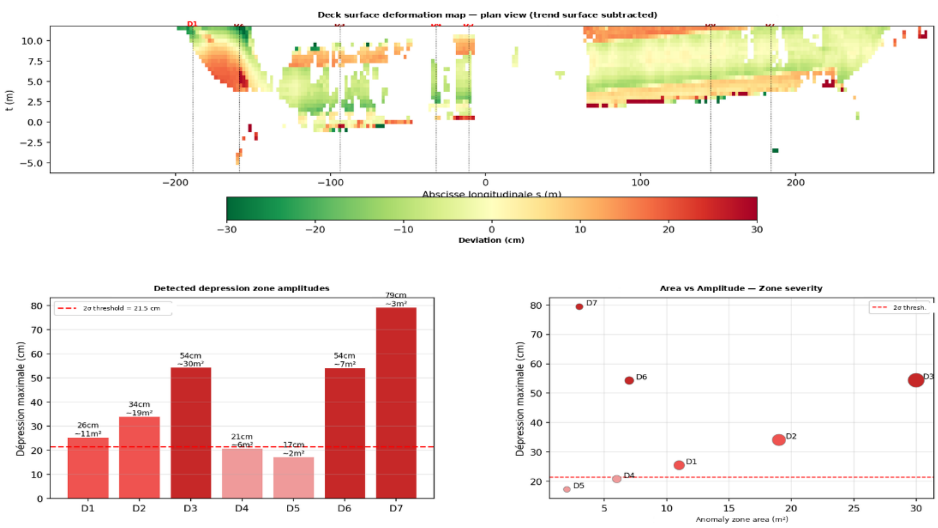

Figure 11. Summary of detected deformation zones. Plan-view residuals map (top), amplitude by zone D1–D7 (bottom left) and amplitude vs. area diagram (bottom right).

3.3. UAV Photogrammetry Capability for Deformation Detection

The results of this campaign show that UAV photogrammetry can effectively serve a structural monitoring role: the vertical accuracy of 0.44 cm (one third of the GSD) remains well below the deformation amplitudes recorded (17 to 79 cm), ensuring a favourable signal-to-noise ratio. Similar accuracy levels are reported by Khaloo et al. (2018) [5] (Z RMSE of 0.5–2 cm on comparable bridges) and by Nex & Remondino (2014) [4], whose review establishes that the vertical accuracy of UAV photogrammetric surveys typically reaches 1–2 times the GSD.

A key advantage of the 2D polynomial regression approach is that it does not require a previously established reference state: the trend surface serves this purpose, provided the deck can be approximated by a second-degree polynomial surface. This assumption holds well for an isostatically supported straight-span bridge such as the Old Cotonou Bridge, where deformations remain local perturbations relative to a regular overall geometry.

The very high point cloud density (383 pts/m^2, against an AASHTO minimum of 10 pts/m^2) is a key contributor to the reliability of the results. With an average of 383 points per 1 m^2 cell, the standard error on the median is of the order of 0.03 mm, well below the systematic photogrammetric uncertainty (0.44 cm). Remondino et al. (2014) [8] showed more generally that Dense Image Matching can rival LiDAR once point density is sufficiently high. It should be noted that only three GCPs were available for this survey (Section 2.2.3), below the six points generally recommended for a rigorous bundle adjustment, and consistent with the broader finding that both the number and spatial distribution of GCPs strongly control the attainable planimetric and vertical accuracy of UAV-SfM surveys [16]. This limitation mainly affects the planimetric component: the RMSE XY of 5.28 cm is markedly higher than the RMSE Z of 0.44 cm, and a degree of scale drift or local bowing across the model cannot be entirely excluded in the absence of additional planimetric control. However, since the deformation analysis presented here relies exclusively on relative vertical deviations within a single, internally consistent block — rather than on absolute planimetric positioning — the conclusions on deck deformation amplitudes and locations remain robust; a denser GCP network would nonetheless be advisable in future campaigns to reduce this residual uncertainty and to allow direct multi-temporal comparison with future surveys.

3.4. Structural Interpretation of Detected Anomalies

Joint examination of the residuals map and the longitudinal and transverse profiles links the seven depression zones (D1–D7) to three distinct mechanisms.

D3, D6 and D7 are attributable to differential settlements at the piers. D3 (s = −94 m, −54.4 cm) and D6 (s = +145 m, −54.3 cm) display nearly identical amplitudes and are located at a spacing consistent with the intermediate pier positions. As for D7, with −79.4 cm over just 3 m^2, it exceeds the structural alert threshold of the AASHTO Manual for Bridge Evaluation and must be classified as the highest priority for intervention.

D1, D2, D4 and D5 show more moderate amplitudes (17 to 34 cm) and limited extents (2 to 19 m^2). Examination of the orthomosaic associates them visually with potholes and localised subsidence of the bituminous wearing course, common on Beninese bridges subjected to repeated overloaded heavy vehicle passages.

The longitudinal profile also reveals a cumulative structural deflection: a systematic level difference of ≈20 cm between mid-span and span-end positions. For comparison, Eurocode 1 sets the admissible deflection for a 12.6 m span at L/800 = 1.6 cm, twelve times lower than the values observed here, signalling a significant loss of global structural stiffness.

These findings are consistent with previous UAV-based investigations of differential settlement and localised deck deterioration reported for other ageing highway structures [15, 20]. Mapping the measured amplitudes against the urgency criteria of the SETRA (1996) and AASHTO (2017) standards, zones D3, D6 and D7 call for urgent structural intervention, while D1, D2, D4 and D5 can be addressed through scheduled routine maintenance.

4. Conclusions

This study has demonstrated that UAV photogrammetry constitutes a quantitative, reproducible and cost-effective tool for the structural inspection of urban bridges in Africa. From 573 images acquired at 56.1 m altitude, processing under Metashape 2.3.1 [10] produced a cloud of 26.8 million classified points (383 pts/m^2), a 1.28 cm/px orthomosaic and a DEM at 5.11 cm/px, with a vertical accuracy of 0.44 cm.

2D polynomial regression surface modelling and statistical analysis of residuals led to the identification of seven depression zones (D1–D7) with amplitudes ranging from −17.3 cm to −79.4 cm over extents of 2 to 30 m^2. Zones D3, D6 and D7 are classified as severe anomalies linked to differential pier settlements. The full set of products — orthomosaic, classified cloud, DEM and deformation map — constitutes the first geometric numerical reference state (T_0) of the Old Cotonou Bridge, a dataset that asset managers can mobilise immediately to set their intervention priorities.

Abbreviations

UAV	Unmanned Aerial Vehicle
SfM	Structure-from-Motion
DEM	Digital Elevation Model

GSD	Ground Sampling Distance
GCP	Ground Control Point
DoD	DEM of Difference
M3C2	Multiscale Model-to-Model Cloud Comparison
RMSE	Root Mean Square Error
AASHTO	American Association of State Highway and Transportation Officials

Acknowledgments

The authors thank the Directorate General of Public Works of Benin for facilitating access to the Old Cotonou Bridge during the UAV survey campaign.

Author Contributions

Kora Farid Carlos Yarou: Conceptualization, Investigation, Methodology, Software, Writing – original draft

Valery Kouandete Doko: Supervision, Conceptualization, Validation, Writing – review & editing

Boris Ganmavo: Resources, Investigation, Data curation, Writing – review & editing

Thede Agbelele: Investigation, Visualization

Mohamed Gibigaye: Project administration, Supervision

Conflicts of Interest

The authors declare no conflicts of interest.

References

[1] Mohan, A., Poobal, S. Crack detection using image processing: a critical review and analysis. *Alexandria Engineering Journal*. 2018, 57(2), 787–798. https://doi.org/10.1016/j.aej.2017.01.020

[2] Colomina, I., Molina, P. Unmanned aerial systems for photogrammetry and remote sensing: A review. *ISPRS Journal of Photogrammetry and Remote Sensing*. 2014, 92, 79–97. https://doi.org/10.1016/j.isprsjprs.2014.02.013

[3] Nex, F., Remondino, F. UAV for 3D mapping applications: a review. *Applied Geomatics*. 2014, 6(1), 1–15. https://doi.org/10.1007/s12518-013-0120-x

[4] Ellenberg, A., Branco, L., Krick, A., Bartoli, I., Kontsos, A. Use of unmanned aerial vehicle for quantitative infrastructure evaluation. *Journal of Infrastructure Systems*. 2015, 21(3), 04014054. https://doi.org/10.1061/(ASCE)IS.1943-555X.0000246

[5] Khaloo, A., Lattanzi, D., Cunningham, K., Dell'Andrea, R., Riley, M. Unmanned aerial vehicle inspection of the Placer River Trail Bridge through image-based 3D modelling. *Structure and Infrastructure Engineering*. 2018, 14(1), 124–136. https://doi.org/10.1080/15732479.2017.1330891

[6] Mlambo, R., Woodhouse, I., Gerard, F., Anderson, K. Structure from Motion (SfM) Photogrammetry with Drone Data: A Low Cost Method for Monitoring Greenhouse Gas Emissions from Forests in Developing Countries. *Forests*. 2017, 8(3), 68. https://doi.org/10.3390/f8030068

[7] Wheaton, J. M., Brasington, J., Darby, S. E., Sear, D. A. Accounting for uncertainty in DEMs from repeat topographic surveys: improved sediment budgets. *Earth Surface Processes and Landforms*. 2010, 35(2), 136–156. https://doi.org/10.1002/esp.1886

[8] Lague, D., Brodu, N., Leroux, J. Accurate 3D comparison of complex topography with terrestrial laser scanner: Application to the Rangitikei canyon (N-Z). *ISPRS Journal of Photogrammetry and Remote Sensing*. 2013, 82, 10–26. https://doi.org/10.1016/j.isprsjprs.2013.04.009

[9] Remondino, F., Spera, M. G., Nocerino, E., Menna, F., Nex, F. State of the art in high density image matching. *The Photogrammetric Record*. 2014, 29(146), 144–166. https://doi.org/10.1111/phor.12063

[10] Agisoft LLC. Agisoft Metashape Professional User Manual, Version 2.3. Saint Petersburg, Russia, 2023.

[11] Bartczak, E. T., Bassier, M., Vergauwen, M. Case study for UAS-assisted bridge inspections. *The International Archives of the Photogrammetry, Remote Sensing and Spatial Information Sciences*. 2023, XLVIII-2/W3-2023, 33–39. https://doi.org/10.5194/isprs-archives-XLVIII-2-W3-2023-33-2023

[12] De Arriba López, V., Maboudi, M., Achanccaray, P., Gerke, M. Automatic non-destructive UAV-based structural health monitoring of steel container cranes. *Applied Geomatics*. 2024, 16(1), 125–145. https://doi.org/10.1007/s12518-023-00542-7

[13] Jin, T., Zhang, W., Chen, C., Chen, B., Zhuang, Y., Zhang, H. Deep-learning- and unmanned aerial vehicle-based structural crack detection in concrete. *Buildings*. 2023, 13(12), 3114. https://doi.org/10.3390/buildings13123114

[14] Maboudi, M., Backhaus, J., Mai, I., Ghassoun, Y., Khedar, Y., Lowke, D., Riedel, B., Bestmann, U., Gerke, M. Very high-resolution bridge deformation monitoring using UAV-based photogrammetry. *Journal of Civil Structural Health Monitoring*. 2025. https://doi.org/10.1007/s13349-025-01001-0

[15] Graves, W., Aminfar, K., Lattanzi, D. Full-Scale Highway Bridge Deformation Tracking via Photogrammetry and Remote Sensing. *Remote Sensing*. 2022, 14(12), 2767. https://doi.org/10.3390/rs14122767

[16] Sanz-Ablanedo, E., Chandler, J. H., Rodríguez-Pérez, J. R., Ordóñez, C. Accuracy of Unmanned Aerial Vehicle (UAV) and SfM Photogrammetry Survey as a Function of the Number and Location of Ground Control Points Used. *Remote Sensing*. 2018, 10(10), 1606. https://doi.org/10.3390/rs10101606

[17] Zollini, S., Alicandro, M., Dominici, D., Quaresima, R., Giallonardo, M. UAV Photogrammetry for Concrete Bridge Inspection Using Object-Based Image Analysis (OBIA). *Remote Sensing*. 2020, 12(19), 3180. https://doi.org/10.3390/rs12193180

[18] Seo, J., Duque, L., Wacker, J. Drone-enabled Bridge Inspection Methodology and Application. *Automation in Construction*. 2018, 94, 112–126. https://doi.org/10.1016/j.autcon.2018.06.006

[19] Chen, S., Laefer, D. F., Mangina, E., Zolanvari, S. M. I., Byrne, J. UAV Bridge Inspection through Evaluated 3D Reconstructions. *Journal of Bridge Engineering*. 2019, 24(4), 05019001. https://doi.org/10.1061/(ASCE)BE.1943-5592.0001343

[20] Hackl, J., Adey, B. T., Woźniak, M., Schümperlin, O. Use of Unmanned Aerial Vehicle Photogrammetry to Obtain Topographical Information to Improve Bridge Risk Assessment. *Journal of Infrastructure Systems*. 2018, 24(1), 04017041. https://doi.org/10.1061/(ASCE)IS.1943-555X.0000393